





Understanding the Synergy between Fe and Mo Sites in the Nitrate Reduction Reaction on a Bio-Inspired Bimetallic MXene Electrocatalyst

Journal Article

Author(s):

[Abbott, Daniel Francis](#) ; [Xu, Yuan-Zi](#); [Kuznetsov, Denis](#) ; [Kumar, Priyank](#); [Müller, Christoph R.](#); [Fedorov, Alexey](#) ; [Mougel, Victor](#) 

Publication date:

2023-12-18

Permanent link:

<https://doi.org/10.3929/ethz-b-000643988>

Rights / license:

[Creative Commons Attribution-NonCommercial-NoDerivatives 4.0 International](#)

Originally published in:

Angewandte Chemie 135(51), <https://doi.org/10.1002/ange.202313746>

Funding acknowledgement:

853064 - Hybrid Electrocatalysts Inspired by the Nitrogenase Enzyme (EC)

Electrocatalysis

Understanding the Synergy between Fe and Mo Sites in the Nitrate Reduction Reaction on a Bio-Inspired Bimetallic MXene Electrocatalyst

Daniel F. Abbott, Yuan-Zi Xu, Denis A. Kuznetsov, Priyank Kumar, Christoph R. Müller,* Alexey Fedorov,* and Victor Mougel*

Abstract: Mo- and Fe-containing enzymes catalyze the reduction of nitrate and nitrite ions in nature. Inspired by this activity, we study here the nitrate reduction reaction (NO₃RR) catalyzed by an Fe-substituted two-dimensional molybdenum carbide of the MXene family, *viz.*, Mo₂CT_x:Fe (T_x are oxo, hydroxy and fluoro surface termination groups). Mo₂CT_x:Fe contains isolated Fe sites in Mo positions of the host MXene (Mo₂CT_x) and features a Faradaic efficiency (FE) and an NH₃ yield rate of 41 % and 3.2 μmol h⁻¹ mg⁻¹, respectively, for the reduction of NO₃⁻ to NH₄⁺ in acidic media and 70 % and 12.9 μmol h⁻¹ mg⁻¹ in neutral media. Regardless of the media, Mo₂CT_x:Fe outperforms monometallic Mo₂CT_x owing to a more facile reductive defunctionalization of T_x groups, as evidenced by *in situ* X-ray absorption spectroscopy (Mo K-edge). After surface reduction, a T_x vacancy site binds a nitrate ion that subsequently fills the vacancy site with O* via oxygen transfer. Density function theory calculations provide further evidence that Fe sites promote the formation of surface O vacancies, which are identified as active sites and that function in NO₃RR in close analogy to the prevailing mechanism of the natural Mo-based nitrate reductase enzymes.

Introduction

Excessive use of nitrogen-rich fertilizers and the unregulated discharge of industrial wastewater have resulted in a significant buildup of nitrate salts in the environment, particularly in groundwater, posing substantial risks to terrestrial and aquatic ecosystems.^[1] Prolonged exposure to high nitrate ion concentrations in drinking water can lead to severe adverse health effects, including cancer and birth defects.^[2] In response, The World Health Organization (WHO) has issued guidelines stipulating a maximum nitrate concentration of 50 ppm NO₃⁻ (11.3 ppm of nitrate-nitrogen, NO₃-N) in safe drinking water.^[3] Nonetheless, even in

developed countries, finding water supplies that adhere to these regulations remains a challenge. This situation underscores the urgent need for scalable and deployable nitrate remediation technologies.^[1,4] Biological denitrification provides an effective method for direct nitrate removal from diverse wastewater sources, but it primarily converts nitrate into dinitrogen gas, bypassing the opportunity to recover the valuable nitrogen. In addition, the formation and release of nitrous oxide as a side product, a 300 times more potent greenhouse gas than carbon dioxide, poses a significant drawback. Alternatively, remediation of nitrate-contaminated waters via reverse osmosis or ion exchange utilizes nitrate displacement rather than chemical conversion.^[5] However, existing technologies are generally considered economically and environmentally unsustainable due to the high rates of sludge production, energy consumption, and the rather low market value of nitrate.^[6]

More recently, denitrification via the electrochemical nitrate reduction reaction (NO₃RR) has been gaining traction due to its ability to utilize electricity from renewable energy sources, thereby providing a pathway towards zero carbon emissions.^[7] The electrochemical transformation of nitrate has focused largely on the reduction of nitrate to gaseous N₂, aiming to close the N₂ cycle.^[7] In the past few years there has been a growing interest in generating ammonia from nitrate to repurpose spent fertilizer and industrial wastewater.^[7-8] This approach, primarily aimed at valorizing the nitrogen content of the feed, can potentially circumvent some of the drawbacks inherent to the nitrate removal strategies introduced above. First, strategies for ammonia separation typically prove to be technically simpler and more energy and economically efficient than those used

[*] Dr. D. F. Abbott, Y.-Z. Xu, Prof. Dr. V. Mougel
Department of Chemistry and Applied Biosciences, ETH Zürich
Vladimir-Prelog-Weg 1–5, 8093 Zürich (Switzerland)
E-mail: mougel@inorg.chem.ethz

Dr. D. A. Kuznetsov, Prof. Dr. C. R. Müller, Dr. A. Fedorov
Department of Mechanical and Process Engineering, ETH Zürich
Leonhardstrasse 21, 8092 Zürich (Switzerland)
E-mail: muelchri@ethz.ch
fedorool@ethz.ch

Dr. P. Kumar
School of Chemical Engineering, University of New South Wales
Sydney
Sydney (Australia)

© 2023 The Authors. *Angewandte Chemie* published by Wiley-VCH GmbH. This is an open access article under the terms of the Creative Commons Attribution Non-Commercial NoDerivs License, which permits use and distribution in any medium, provided the original work is properly cited, the use is non-commercial and no modifications or adaptations are made.

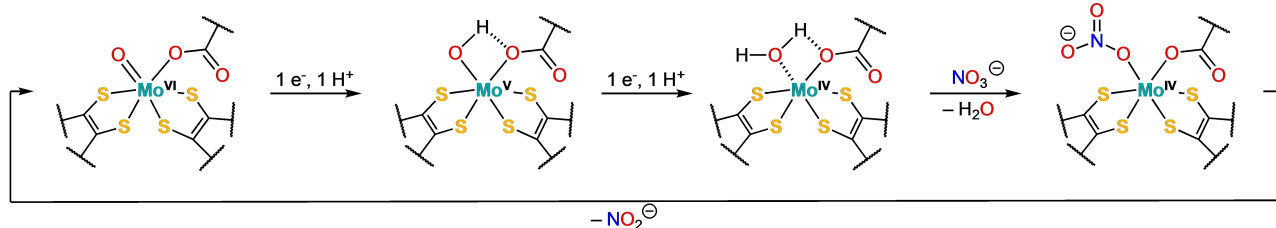
for nitrate separation.^[9] Second, the market value of ammonia considerably surpasses that of nitrate. Consequently, such strategies hold the potential to valorize nitrogen contained in waste sources while subsequently reducing our dependency on the highly energy intensive Haber-Bosch process.^[10]

The conversion of nitrate to ammonia is a complex, 8 electron, 9 proton reduction sequence that involves several intermediates. Nature relies on a series of enzymes that enable these successive reductions. First, the two-electron reduction of nitrate to nitrite occurs in neutral media via nitrate reductase enzymes (NRases).^[10b,11] Various NRases have been reported to feature a mononuclear molybdenum active site coordinated by four sulfur atoms from two pyranopterin ligands. The key steps in the nitrate reduction by respiratory NRases are two subsequent proton coupled electron transfer (PCET) steps of the parent Mo^{VI} oxo active site, enabling the formation of a transient Mo^V hydroxo species, which is then further reduced and protonated to a Mo^{IV} aquo complex (Scheme 1a). The aquo ligand is bound only weakly and its dissociation generates a coordinatively unsaturated Mo center that binds an oxygen atom from a nitrate anion and initiates its reduction to a nitrite anion via an oxygen atom transfer to Mo^{IV}.^[11–12] Subsequently, the six-electron reduction of a nitrite anion to an ammonium cation can be catalyzed by cytochrome *c* nitrite reductase (NrfA) enzymes.^[13] The active site in those enzymes is an Fe heme site coordinated by an amine group of lysine in the proximal axial position, while the distal axial coordination site is free to interact with substrates such as nitrite and hydroxylamine species.^[13–14] Previous studies have sought to mimic the active sites of NRases and NrfA enzymes through the development of bio-inspired electrocatalysts. For example, the oxo-containing molybdenum sulfide (oxo-MoS_x) exploits a Mo site that is coordinated by oxo and thiolate ligands, effectively mimicking the active center of NRases.^[15] Oxo-MoS_x was shown to generate NH₄⁺ via NO₃RR at 0 V and

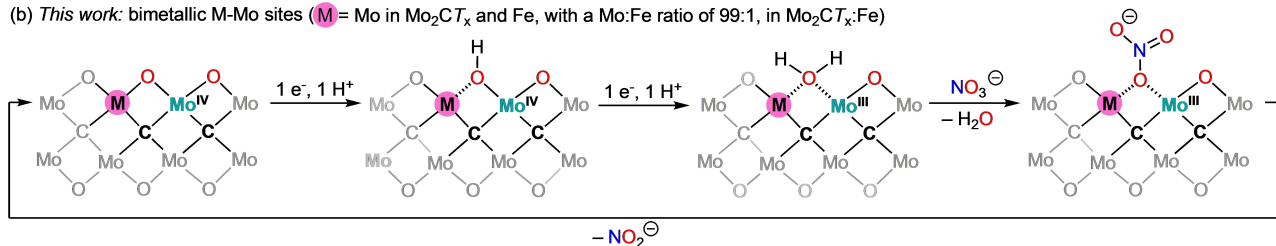
–0.1 V with a Faradaic efficiency (FE) of ca. 96 % and 50 %, respectively, and with average current densities of 31 and 107 μA cm⁻². Similarly, inspired by the heme centers of various reductase enzymes, electrocatalysts featuring highly-dispersed (down to a single atom) active sites based on Fe, Co, and other metals have shown promise for reducing nitrate^[8c] and nitrite ions,^[16b,17] as well as nitrous oxide.^[18]

Recent studies have demonstrated that MXenes, a rapidly developing class of two-dimensional (2D) carbides, nitrides and carbonitrides based on early transition metals, are promising catalysts for various electrocatalytic reactions due to a high degree of control over the structure of their surface sites.^[19] In particular, the electronic structure and catalytic properties of MXenes are tunable by metal substitution in the lattice of the parent carbide, allowing for the generation of active sites tailored to a specific application, such as Co-substituted Mo-based MXene, Mo₂CT_x:Co (T_x=O, OH, F surface terminations) for the hydrogen evolution reaction (HER).^[20] An alternative synthetic approach to MXene-based single-atom catalysts (SACs)^[21] is to rely on the use of MXenes as supports to confine atomically-dispersed late transition metals (Pt, Ru) to surface defects (metal vacancies) in the host MXene phases.^[22] However, precise control over the speciation (SACs, dimers, trimers, clusters, etc.) of the active site in such post-synthetically modified MXenes is challenging.^[23] From this standpoint, the substitution of metal sites of a parent MXene is an attractive (yet understudied) approach to generate SACs. Towards this end, we have recently reported the preparation of an Fe-substituted Mo-based MXene, Mo₂CT_x:Fe, and disclosed the instability of this material (as well as that of various other MXenes) in strongly basic media.^[24] Yet, since Mo₂CT_x:Fe remains structurally stable in neutral and acidic media, the exploration of this material for the NO₃RR is appealing owing to the presence of isolated Fe sites in close proximity to Mo sites and because the combination of these metals is known to facilitate the NO₃RR in naturally

(a) Nitrate reductase enzymes (Mo^{VI}/Mo^{IV} redox)



(b) This work: bimetallic M-Mo sites (M = Mo in Mo₂CT_x and Fe, with a Mo:Fe ratio of 99:1, in Mo₂CT_x:Fe)



Scheme 1. Proposed NO₃RR mechanism for (a) natural nitrate reductases and (b) the MXene materials studied in this work. Charges are omitted for brevity.

occurring nitrate and nitrite reductase enzymes. In general, MXenes have remained underexplored as electrocatalysts for the nitrate reduction reaction.^[25]

Expanding upon our prior work, which examined the use of $\text{Mo}_2\text{CT}_x\text{:Fe}$ as a precursor for an active electrocatalyst promoting the oxygen reduction reaction, we report here that $\text{Mo}_2\text{CT}_x\text{:Fe}$ displays by itself a high activity and selectivity for the reduction of nitrate ions to ammonia. The activity and selectivity of $\text{Mo}_2\text{CT}_x\text{:Fe}$ is higher than that of the unsubstituted Mo_2CT_x both in acidic and neutral media.

Leveraging advanced *in situ* X-ray absorption spectroscopy (Mo K-edge), we provide a detailed examination of the electronic and local structure of the working MXene catalysts. The results reveal that the substitution of Mo with Fe in the Mo_2CT_x lattice facilitates the formation of under-coordinated Mo sites via the reductive defunctionalization of surface terminating groups (T_x). In other words, the substitution of Mo by Fe promotes the reducibility (deoxygenation) of the MXene surface, which is key to a higher ammonia selectivity and activity in acidic and neutral media, involving steps presented in Scheme 1b. In accordance with experimental observations, DFT calculations reveal that formation of oxygen vacancies precedes $\text{NO}_3^-/\text{NO}_2^-$ adsorption steps and this step is less endergonic on a Fe-substituted model surface versus a non-substituted surface. Overall, the results presented herein demonstrate how the activity and selectivity of Mo_2CT_x can be effectively tailored to favor the formation of NH_3 via the partial substitution of Mo by Fe,

creating an active site reminiscent of the natural Mo-based nitrate reductase enzymes, and serving as a roadmap to the further development of MXenes for NO_3RR .

Results and Discussion

Owing to a higher availability of protons for the PCET steps at a low pH, as well as a higher reactivity of HNO_3 relative to the nitrate anion, NO_3^- ,^[26] we first investigated $\text{Mo}_2\text{CT}_x\text{:Fe}$, using the same batch of a material described by us previously with 0.42 wt % Fe,^[24] with regards to its electrochemical NO_3RR activity in acidic media (0.05 M H_2SO_4) with and without the addition of 100 mM NO_3^- (from NaNO_3). In addition, Mo_2CT_x , a reported material,^[27] was evaluated under the same conditions in order to probe the influence of Fe substitution. The linear sweep voltammograms (LSVs) are depicted in Figure 1a. When comparing the nitrate reduction curves of $\text{Mo}_2\text{CT}_x\text{:Fe}$ to those without the addition of nitrate ions (i.e., NO_3RR vs. blank), the onset of NO_3RR can be assigned to a potential of ca. $-0.05 \text{ V}_{\text{RHE}}$. Further, the current continues to decrease gradually until ca. $-0.3 \text{ V}_{\text{RHE}}$, at which point the current in both curves decreases rapidly, owing to the dominant HER at these potentials. On the other hand, we observe that the current of the blank and NO_3RR curves remain nearly superimposable for Mo_2CT_x until the onset of HER at ca.

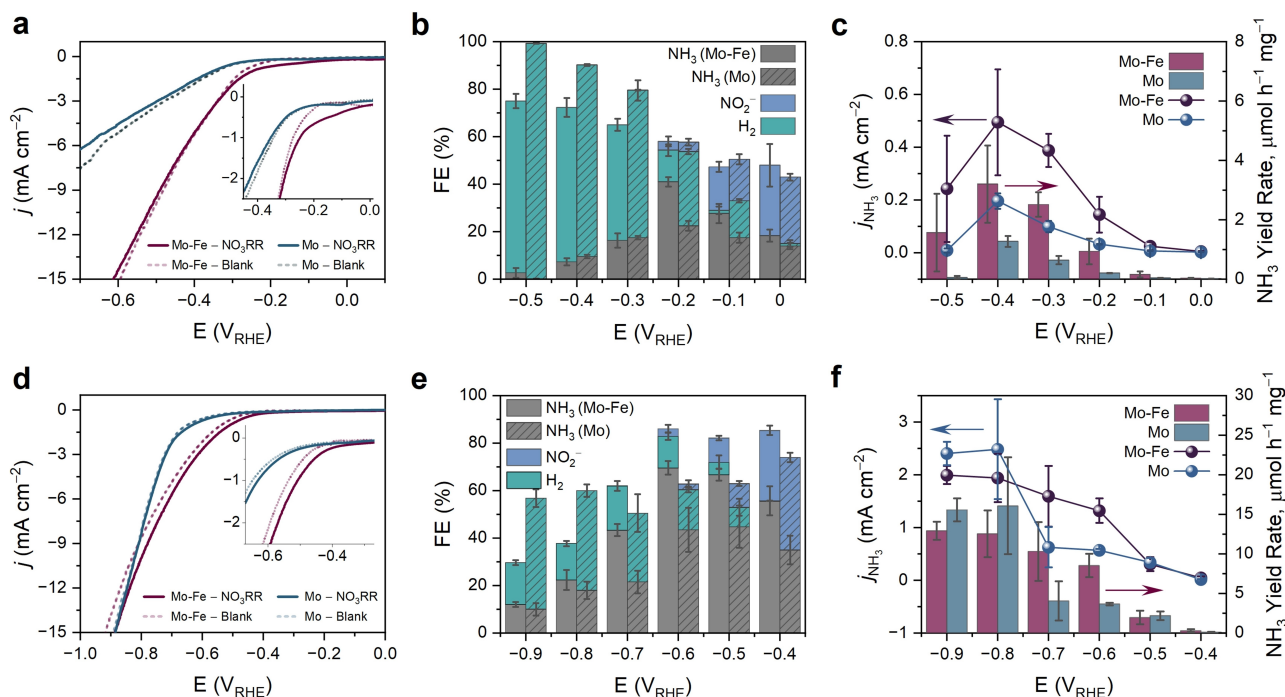


Figure 1. (a) Linear sweep voltammograms ($v = 5 \text{ mV s}^{-1}$) of $\text{Mo}_2\text{CT}_x\text{:Fe}$ and Mo_2CT_x in 0.05 M H_2SO_4 with and without the addition of 100 mM NO_3^- in solution as well as (b) the Faradaic efficiencies of all quantified products after 1 h of CA experiments at each potential, and (c) the partial current densities for NH_3 and the NH_3 yield rates at each CA potential in 0.05 M H_2SO_4 . (d) Linear sweep voltammograms ($v = 5 \text{ mV s}^{-1}$) of $\text{Mo}_2\text{CT}_x\text{:Fe}$ and Mo_2CT_x in 0.5 M Na_2SO_4 with and without the addition of 100 mM NO_3^- in solution as well as (e) the Faradaic efficiencies of all quantified products after 1 h of CA experiments at each potential, and (f) the partial current densities for NH_3 and the NH_3 yield rates at each CA potential in 0.5 M Na_2SO_4 .

$-0.3 V_{\text{RHE}}$, implying a notably lower NO_3RR activity for this material.

Chronoamperometric (CA) hold experiments were then performed over the range of 0 to $-0.5 V_{\text{RHE}}$ to examine the NO_3RR activity and ammonia selectivity in greater detail (Figures S1–S2). Figure 1b–c presents the corresponding FE, partial current densities (j_{NH_3}), and NH_3 yield rates for $\text{Mo}_2\text{CT}_x\text{:Fe}$ and Mo_2CT_x (0.05 M H_2SO_4). In general, both $\text{Mo}_2\text{CT}_x\text{:Fe}$ and Mo_2CT_x demonstrate a comparable selectivity towards NO_2^- and NH_3 at the onset of NO_3RR at 0 V_{RHE} , reaching FE values of ca. 29% and 14–18%, respectively. However, as the applied potential is decreased, the product selectivity shifts mainly towards NH_3 at intermediate potentials and ultimately towards H_2 at low potentials, with the FE_{NH_3} peak occurring at ca. $-0.2 V_{\text{RHE}}$ (Figure 1b). Interestingly, we observe that at $-0.2 V_{\text{RHE}}$, the FE towards NH_3 (FE_{NH_3}) on $\text{Mo}_2\text{CT}_x\text{:Fe}$ is nearly double that of Mo_2CT_x (41% and 22%, respectively). More importantly, $\text{Mo}_2\text{CT}_x\text{:Fe}$ consistently reaches higher NH_3 yield rates and partial current densities than Mo_2CT_x across the entire potential range examined, reaching a peak NH_3 yield rate of $3.2 \mu\text{mol h}^{-1} \text{mg}^{-1}$ at $-0.4 V_{\text{RHE}}$, which is more than twice that of Mo_2CT_x ($1.3 \mu\text{mol h}^{-1} \text{mg}^{-1}$, Figure 1c).

In order to confirm that the detected NH_3 originated from NO_3^- ions in solution, the CA experiments were repeated using isotope-labelled $^{15}\text{NO}_3^-$. Indeed, comparable NH_3 yield rates were obtained for both $^{14}\text{NO}_3^-$ and $^{15}\text{NO}_3^-$ ions and the ^1H NMR spectra of the produced ammonium show a triplet for $^{14}\text{NH}_4^+$ and a doublet for $^{15}\text{NH}_4^+$, both of which are consistent with the occurrence of NO_3RR (Figure S3). In addition, no NH_3 was detected during the blank experiments that contained no NO_3^- (Figure S3), and no significant Fe leaching was observed in acidic conditions (See Supporting Information for details). Overall, the above findings highlight the influence of Fe substitution in Mo_2CT_x on the selectivity to ammonia under NO_3RR conditions and on the ammonia yield rates, *viz.* while Mo_2CT_x shows a high catalytic activity for HER and reaches 100% FE_{H_2} at -0.5 V , consistent with reports on the high efficiency of Mo_2CT_x for HER,^[20,28] $\text{Mo}_2\text{CT}_x\text{:Fe}$ features a notable increase in the NO_3RR activity and selectivity towards NH_3 relative to Mo_2CT_x , suggesting that Fe plays an important role in enabling the reduction of NO_3^- to NH_3 in acidic media.

The development of NO_3RR electrocatalysts active in neutral media is vital considering that contaminated water sources typically have a near-neutral pH.^[7] In addition, exploring the NO_3RR in neutral electrolytes is essential to elucidate the effects of pH on the activity and selectivity of the electrocatalysts. As discussed above, alkaline NO_3RR conditions were not explored due to the known structural instability of $\text{Mo}_2\text{CT}_x\text{:Fe}$ and other MXenes at high pH (under aerobic conditions).^[24] Therefore, next we evaluated the NO_3RR performances of $\text{Mo}_2\text{CT}_x\text{:Fe}$ and Mo_2CT_x in neutral media using 0.5 M Na_2SO_4 as the electrolyte (pH = 7). The LSVs for both materials recorded in the absence and presence of NO_3^- are compared in Figure 1d. The onset for NO_3RR is identified clearly at ca. $-0.4 V_{\text{RHE}}$ for $\text{Mo}_2\text{CT}_x\text{:Fe}$ as the deviation of the LSV curve from that of the blank.

We note that NO_3RR proceeds on both materials until roughly $-0.9 V_{\text{RHE}}$. Chronoamperometry was performed in the $-0.4 V_{\text{RHE}}$ to $-0.9 V_{\text{RHE}}$ potential region (Figure S4) and the corresponding FE's are presented in Figure 1e. Similar to the results in acidic media, NO_2^- and NH_3 are the primary products detected near the NO_3RR onset at $-0.4 V_{\text{RHE}}$. However, on $\text{Mo}_2\text{CT}_x\text{:Fe}$ the FE_{NH_3} has improved reaching up to 56% and only up to 35% on Mo_2CT_x at $-0.4 V_{\text{RHE}}$. As the potential is decreased further, the FE_{NH_3} on $\text{Mo}_2\text{CT}_x\text{:Fe}$ continues to increase, reaching 70% at $-0.6 V_{\text{RHE}}$, which is ca. 1.5 times higher than that of Mo_2CT_x under identical conditions and exceeds the peak FE_{NH_3} reached by $\text{Mo}_2\text{CT}_x\text{:Fe}$ in acidic media (41%). Blank experiments and $^{15}\text{NO}_3^-$ labeling confirm that all detected NH_3 originates from NO_3RR (Figure S5).

Overall, the competition from HER is reduced notably in neutral media relative to acidic media on both $\text{Mo}_2\text{CT}_x\text{:Fe}$ and Mo_2CT_x , which is attributed to the low concentration of protons at pH = 7. Interestingly, the FE_{H_2} on $\text{Mo}_2\text{CT}_x\text{:Fe}$ is relatively stable across most of the potentials examined ($-0.6 V_{\text{RHE}}$ to $-0.9 V_{\text{RHE}}$). In contrast to acidic media, the total FE ($\text{NH}_3 + \text{H}_2 + \text{NO}_2^-$) remains below 60% at high overpotentials, e.g. at $-0.8 V_{\text{RHE}}$. We hypothesize that the low total FE at high overpotentials originates from a competing formation of N_2 , which was observed as a reaction product under these conditions by gas chromatography. However, the quantification of N_2 at the low concentrations detected in this work proved to be a significant challenge within our set up. The difficulty was not rooted in the precision of the gas chromatography (helium ionization detection technique was used), but rather in the separation of trace amounts of electrogenerated N_2 from minor yet more significant amounts of residual N_2 in the argon gas feed used to purge the H-cell. Therefore, FE_{N_2} is not reported here.

The NH_3 yield rates and partial current densities for $\text{Mo}_2\text{CT}_x\text{:Fe}$ and Mo_2CT_x are shown in Figure 1f. Under neutral pH conditions, the NO_3RR activity towards NH_3 has improved notably relative to acidic media. Specifically, $\text{Mo}_2\text{CT}_x\text{:Fe}$ reaches a maximum FE_{NH_3} of 70% and a yield rate of $12.9 \mu\text{mol h}^{-1} \text{mg}^{-1}$ in neutral media (at $-0.6 V_{\text{RHE}}$) while a FE_{NH_3} of only 41% and a yield rate of $3.2 \mu\text{mol h}^{-1} \text{mg}^{-1}$ are obtained in acidic media (at $-0.2 V_{\text{RHE}}$). The higher FE_{NH_3} and yield rates observed in neutral vs. acidic media, resulting from the disfavored HER at low proton concentration, however, come at the cost of a higher onset overpotential, as acidic media favors the formation of HNO_3 , a more easily reducible species than NO_3^- .^[26]

The high FE_{NH_3} of $\text{Mo}_2\text{CT}_x\text{:Fe}$ in neutral media is also shown to remain stable over the course of a series of ten 2-hour potential holds at $-0.6 V_{\text{RHE}}$, demonstrating the high recyclability of the catalyst (Figure S6a). When probing the long-term stability of $\text{Mo}_2\text{CT}_x\text{:Fe}$ under constant potential, we observed that FE_{NH_3} decreases by ca. 12% over the course of 13 h (Figure S6b). We hypothesize that in such a non-buffered system, this can be attributed to changes in pH, which was observed to shift from neutral (pH 7) to alkaline (pH 13) due to the *in situ* generation of ammonium

hydroxide. This pH increase may consequently result in catalyst degradation, as our previous studies have shown that $\text{Mo}_2\text{CT}_x\text{:Fe}$ is unstable in strongly alkaline conditions and evolves to iron oxyhydroxide dispersed on graphitic carbon (in the presence of oxygen).^[24] Interestingly, the difference in the FE_{NH_3} between $\text{Mo}_2\text{CT}_x\text{:Fe}$ and Mo_2CT_x in neutral media is not as stark as it is in acidic media. In general, we observe that $\text{Mo}_2\text{CT}_x\text{:Fe}$ and Mo_2CT_x show comparable performance at less negative potentials, but $\text{Mo}_2\text{CT}_x\text{:Fe}$ shows considerably higher partial current densities and more than double the NH_3 yield rate at more negative potentials (i.e. -0.6 and $-0.7 \text{ V}_{\text{RHE}}$). $\text{Mo}_2\text{CT}_x\text{:Fe}$ and Mo_2CT_x again show a similar performance as the potential is decreased below $-0.8 \text{ V}_{\text{RHE}}$. Considering that the FE_{H_2} on $\text{Mo}_2\text{CT}_x\text{:Fe}$ is ca. half that of Mo_2CT_x and that the FE towards the detected products ($\text{NH}_3 + \text{H}_2 + \text{NO}_2^-$) reported in Figure 1e is below 40% at $\leq -0.8 \text{ V}_{\text{RHE}}$, we infer that $\text{Mo}_2\text{CT}_x\text{:Fe}$ still shows a higher activity for NO_3RR than Mo_2CT_x and that the selectivity instead shifts to N_2 at highly negative potentials. The higher overall j_{NH_3} and NH_3 yield rate observed on Mo_2CT_x , however, may be related to the lower unit cell parameter of $\text{Mo}_2\text{CT}_x\text{:Fe}$ ($c = 20.407(2) \text{ \AA}$) relative to that of the unsubstituted Mo_2CT_x ($c = 20.567(1) \text{ \AA}$).^[20,24, 27b] The lower unit cell parameter c for $\text{Mo}_2\text{CT}_x\text{:Fe}$ may result from the harsher conditions for the etching of Ga from $\text{Mo}_2\text{Ga}_2\text{C:Fe}$ relative to $\text{Mo}_2\text{Ga}_2\text{C}$. In general, the lower unit cell parameter c in $\text{Mo}_2\text{CT}_x\text{:Fe}$ results in a decreased interlayer volume such that at high overpotentials/high current densities, where the effect of mass transport of the products on the reaction rate is particularly pronounced, the observed activity of $\text{Mo}_2\text{CT}_x\text{:Fe}$ can be inferior to that of Mo_2CT_x .

The high NO_3RR activity of $\text{Mo}_2\text{CT}_x\text{:Fe}$ in neutral media and its selectivity towards NH_3 makes this catalyst a prime candidate for the direct and complete conversion of nitrate to ammonia in contaminated water. We hence examined the feasibility of $\text{Mo}_2\text{CT}_x\text{:Fe}$ to selectively reduce nitrate to ammonia from contaminated tap water containing low concentrations of nitrate (10 ppm NO_3^- -N, i.e. 44.3 ppm NO_3^-) without any additional electrolyte (Figure S7a). Note that the chosen concentration of 10 ppm N- NO_3^- is comparable to the recommended WHO guideline for safe drinking water of 50 ppm NO_3^- .^[2] The NH_3 yield rates and FE's for NO_3RR products in tap water containing 10 ppm NO_3^- -N and the corresponding CA curves are shown in Figure S7b-c. Under these conditions, a FE_{NH_3} of up to 70% is achieved with an NH_3 yield rate of $0.73 \mu\text{mol h}^{-1} \text{ mg}^{-1}$ at $-0.4 \text{ V}_{\text{RHE}}$. Blank experiments performed in the absence of NO_3^- while holding the potential at $-0.4 \text{ V}_{\text{RHE}}$ for 2 h showed no detectable amounts of NH_3 (Figure S8a). In addition, control experiments using $^{15}\text{NO}_3^-$ show the formation of $^{15}\text{NH}_3$, consistent with NO_3RR , and allowing to exclude the possibility of contamination by adventitious ammonia (Figure S8b). The effectiveness of $\text{Mo}_2\text{CT}_x\text{:Fe}$ for complete nitrate conversion is further demonstrated in Figure S7d, which highlights that all of the initial NO_3^- contamination is converted to NH_3 over 16 h (at $-0.4 \text{ V}_{\text{RHE}}$).

To summarize, $\text{Mo}_2\text{CT}_x\text{:Fe}$ outperforms Mo_2CT_x in both acidic and neutral media, displaying substantial improve-

ments in the FE_{NH_3} and partial current density towards NH_3 . These electrochemical results demonstrate the advantages of Fe-substitution in the structure of the parent Mo_2CT_x MXene for NO_3RR . To rationalize the origin of this catalytic enhancement by Fe sites and to gain a molecular understanding of the role of the two metal centers (Mo–Mo and Mo–Fe) in the NO_3^- reduction cycle, X-ray absorption spectroscopy was employed to probe the electronic and local structures of Mo sites under the electrocatalytic conditions relevant for NO_3RR .

Figure 2a shows the Mo K-edge *in situ* X-ray absorption near edge spectra (XANES) recorded for $\text{Mo}_2\text{CT}_x\text{:Fe}$ in acidic electrolyte under blank and NO_3RR conditions (i.e. with 0 mM or with 100 mM NO_3^- in solution, respectively). Under blank conditions, the edge position of $\text{Mo}_2\text{CT}_x\text{:Fe}$ is

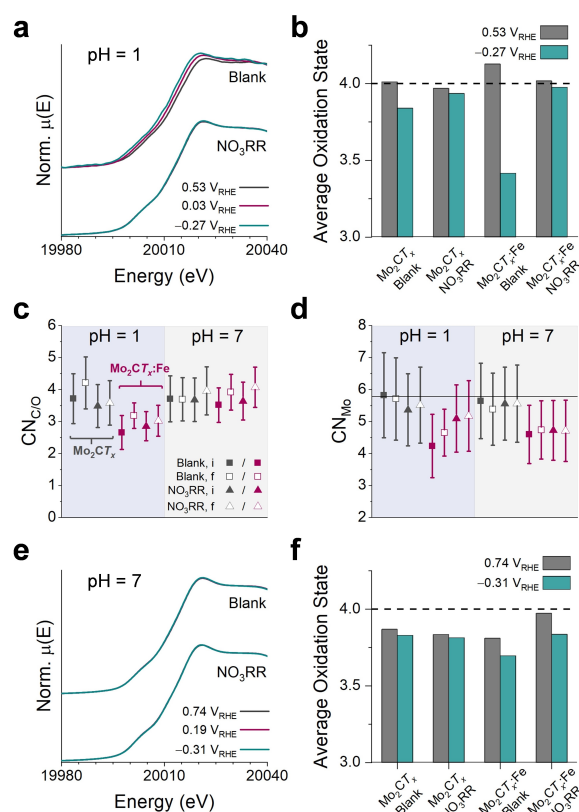


Figure 2. (a) The normalized *in situ* XANES spectra for $\text{Mo}_2\text{CT}_x\text{:Fe}$ in 0.05 M H_2SO_4 recorded under blank and NO_3RR conditions (0 mM and 100 mM NO_3^- , respectively); (b) the oxidation state of $\text{Mo}_2\text{CT}_x\text{:Fe}$ and Mo_2CT_x at the initial ($0.53 \text{ V}_{\text{RHE}}$) and final ($-0.27 \text{ V}_{\text{RHE}}$) applied potentials in 0.05 M H_2SO_4 ; (c) Mo–O/C and (d) Mo–Mo coordination numbers as determined from fitting the FT-EXAFS data. Black symbols indicate the fitting results for Mo_2CT_x and red symbols indicate those for $\text{Mo}_2\text{CT}_x\text{:Fe}$. As specified in the Figure legend, square symbols (\blacksquare) are under blank conditions (0 mM NO_3^-) and triangle symbols (\blacktriangle) are under NO_3RR conditions (100 mM NO_3^-). Filled symbols (e.g. \blacksquare) indicate the initial potential (i.e. OCP) and empty symbols (e.g. \square) are the final potential where NO_3RR occurs (see Tables S1 and S2 for potential values); (e) the normalized *in situ* XANES spectra for $\text{Mo}_2\text{CT}_x\text{:Fe}$ in 0.5 M Na_2SO_4 ; and (f) the oxidation state of $\text{Mo}_2\text{CT}_x\text{:Fe}$ and Mo_2CT_x at the initial ($0.74 \text{ V}_{\text{RHE}}$) and final ($-0.31 \text{ V}_{\text{RHE}}$) applied potentials in 0.5 M Na_2SO_4 .

20011.6 eV at the starting potential of 0.53 V_{RHE}. This edge position corresponds to an average oxidation state of Mo of +4, which is consistent with our previous XANES data for Mo₂CT_x,^[27a,b] as well as the X-ray photoelectron spectroscopy characterization of Mo₂CT_x:Fe.^[24] As the potential is reduced to -0.27 V_{RHE} (i.e., a potential for which NO₃RR/HER was shown to occur in acidic media, see above; Figure S9a), the absorption edge shifts by 2 eV to lower energies (20009.6 eV) (Figure 2a). This shift corresponds to the partial reduction of Mo^{IV} sites to Mo^{III}/Mo^{II} sites. Interestingly, the edge position does not shift from its initial position (20011.3 eV) under NO₃RR conditions. A similar trend is observed for Mo₂CT_x, although the extent of the reduction is lower in the absence of nitrate ions, i.e., the edge positions of Mo₂CT_x are 20011.3 eV and 20010.9 eV at 0.53 V_{RHE} and -0.27 V_{RHE}, respectively, corresponding to only a minor change of the average oxidation state of Mo from +4 to +3.8 (Figure 2b and Figure S10a). Therefore, the presence of Fe sites in Mo₂CT_x modifies the electronic structure of Mo sites by facilitating their electro-reduction. The stability of the absorption edge under NO₃RR conditions for both MXenes implies that NO₃⁻ ions act as an oxidizing agent for the partially reduced (defunctionalized) MXene surface, thereby preventing the reduction of Mo^{IV} sites. Considering that in the non-defunctionalized MXene Mo resides in a coordinatively saturated distorted octahedral environment, the (transient) formation of an O (*T_x*) vacancy (*V_o*) at the Mo site enables the binding of NO₃⁻ and the subsequent oxidation of the formed Mo-*V_o*-M sites (M = Mo, Fe) at the applied potentials. This observation hints at Mo being a part of the NO₃RR active site in both Mo₂CT_x and Mo₂CT_x:Fe catalysts (Scheme 1b).

To further explore the reductive defunctionalization of our catalysts, we analyzed the respective Fourier-transformed (FT) extended X-ray absorption fine structure (EXAFS) spectra (Figure S11). The FT-EXAFS spectra display two main peaks at ca. 1.6 and 2.6 Å. According to reported data,^[27b] the first peak corresponds to six nearest neighboring C/*T_x* (*T_x* = O/OH/F) atoms at interatomic distances of ca. 2.06 Å (for Mo–O/OH/F) and 2.17 Å (for Mo–C). The second peak corresponds to a Mo–Mo coordination shell containing six nearest neighboring Mo atoms at distances of 2.88 Å. Fitting of the *in situ* FT-EXAFS spectra collected in acidic electrolyte (Figures S12–S13 and Table S1) reveals that changes to the catalyst structure due to the applied potential are mostly related to changes in the coordination numbers in the first and second shells (Figure 2c–d), while the bonding distances (Figure S14a–b) and Debye–Waller factors (Figure S14c–d) remain nearly unchanged (Table S1). Fitting of the first shell was performed using a single scattering path to describe the 6 nearest C and O atoms (3 C and 3 O), which yielded coordination numbers (CN_{C/O}) ranging from 3 to 4 with average bonding distances of ca. 2.06–2.07 Å. The CN_{C/O} values for both Mo₂CT_x and Mo₂CT_x:Fe measured *in situ* are lower than those of the pristine model used for the fitting, which strongly indicates that both MXene surfaces are partially defunctionalized and therefore have a lower coverage of surface *T_x* groups than in the pristine model. The defunctionalization (partial or

complete) of *T_x* groups has been observed previously when treating Mo₂CT_x with H₂ at elevated temperatures.^[27a] In the presence of an aqueous electrolyte, however, the availability of protons may facilitate the defunctionalization of the surface oxo/hydroxo groups via the formation of weakly-bound aquo ligands (PCET mechanism). We also note that Mo₂CT_x:Fe features a lower average CN_{C/O} (i.e., lower *T_x* coverage) than Mo₂CT_x under the electrochemical conditions examined (Table S1). This suggests that the substitution of Mo sites by Fe facilitates the formation of surface vacancies in acidic media (i.e. the reduction of Mo sites via the reductive defunctionalization of *T_x* groups), in agreement with *in situ* XANES results (Figure 2a).

The EXAFS fits of the second coordination shell show that Mo₂CT_x:Fe also features lower Mo–Mo coordination numbers (CN_{Mo}) than Mo₂CT_x (Figure 2d). This may be due to the presence of Fe in Mo positions introducing additional disorder into the MXene structure that results in a larger distribution in the Mo–Mo scattering path length. Overall, the combination of lower CN_{C/O} and CN_{Mo} suggests that Mo₂CT_x:Fe generally features a higher number of under-coordinated Mo sites compared to Mo₂CT_x in the conditions studied here. This could be explained by the filling of *T_x* vacancies under electrocatalytic conditions, as can be observed by the increase in CN_{C/O} when transitioning from OCP (i.e. 0.53 V_{RHE}) to a reducing potential (i.e. -0.27 V_{RHE}). However, increasing *T_x* coverage would imply Mo oxidation, yet we observe that under NO₃RR conditions the average oxidation state of Mo does not change or even decreases under blank conditions. Instead, a more likely scenario is that the substrate or reaction intermediates (e.g. HNO₃/NO₃⁻, NO₂⁻, NO) coordinate to the surface Mo atoms under the applied reducing potentials, thereby increasing the CN_{C/O} while avoiding Mo oxidation. Note that the reduction of Mo is only observed under blank conditions in acidic media. We hypothesize that the ease of protonation of the surface *T_x* (oxo or hydroxo) groups in acidic electrolyte to weaker field aquo ligands, that could also easily be de-coordinated, facilitates the reduction of the Mo centers.

Next, we probed the electronic and local structure of Mo in neutral media to rationalize the pH-dependency of the NO₃RR mechanism. Figure 2e compares the *in situ* XANES spectra for Mo₂CT_x:Fe in 0.5 M Na₂SO₄. Tracking of the edge position as a function of the applied potential reveals that the reduction of Mo is significantly hindered in neutral pH regardless of whether NO₃⁻ is present in solution or not (Figure 2e and Figure S9b). Similar results are observed also for Mo₂CT_x (Figure S10b). The average Mo oxidation in all cases remains around +3.8, indicating that the ratio between co-existing Mo^{IV} and Mo^{III}/Mo^{II} sites remains relatively stable, regardless of the applied potential for both Mo₂CT_x:Fe and Mo₂CT_x (Figure 2f). This is in contrast to the observations made in acidic media, in which Mo was found to be in a slightly more oxidized state (ca. +4) at the starting potentials and it would only reach comparable reduced states (i.e. ca. +3.8 for Mo₂CT_x and ca. +3.4 for Mo₂CT_x:Fe) under an applied potential and in the absence of nitrate. Based on these observations, it appears that the ease of reduction of the Mo centers is enhanced in acidic

media, suggesting that Mo reduction indeed proceeds through the protonation of surface O/OH groups. In acidic conditions, the average oxidation state of Mo in both $\text{Mo}_2\text{CT}_x:\text{Fe}$ and Mo_2CT_x is higher than that at neutral pH (Figures 2b and 2f), likely due to the protonation of the oxo T_x groups (O^{2-}) in acidic media and the subsequent protonation-induced increase of the surface density of T_x groups (mostly, hydroxyls).

The corresponding FT-EXAFS spectra are shown in Figure S15, which also exhibit only minor changes under an applied potential. Fitting the EXAFS spectra collected in neutral media (Figures S16–S17 and Table S2) reveal comparable first shell coordination numbers for $\text{Mo}_2\text{CT}_x:\text{Fe}$ and Mo_2CT_x to those in acidic media and also show that $\text{CN}_{\text{C/O}}$ increased slightly under an applied reducing potential (Figure 2c), suggesting the coordination of solvent/electrolyte molecules with the surface under reducing conditions. Extending the fit to the second coordination shell shows again that $\text{Mo}_2\text{CT}_x:\text{Fe}$ consistently features CN_{Mo} values roughly 1 unit lower than Mo_2CT_x (Figure 2d). This indicates that the $\text{Mo}_2\text{CT}_x:\text{Fe}$ structure is more disordered and features a higher fraction of under-coordinated Mo atoms in neutral media.

We note that the low concentration of Fe in $\text{Mo}_2\text{CT}_x:\text{Fe}$ (ca. 0.4 wt % Fe), the high absorption coefficient of Mo, and attenuation of the beam by the electrolyte layer make the measurement of *in situ* XAS data at the Fe K-edge particularly challenging. Therefore, the collection of XANES data at the Fe K-edge was successful only partially, when using an acidic electrolyte under NO_3RR conditions, and provided only a weak XANES signal (Figure S18). That being said, the XANES data collected under these conditions (i.e. 0.05 M H_2SO_4 + 100 mM NO_3^- ; 0.53 V_{RHE} to $-0.27 V_{\text{RHE}}$) agree well with our previously published results for as-prepared $\text{Mo}_2\text{CT}_x:\text{Fe}$, and indicate that Fe is in an average oxidation state close to +2, as suggested by the location of the edge position at ca. 7120 eV.^[24] Interestingly, we can identify a slight shift in the Fe edge position and a

development of the pre-edge feature at ca. 7122 eV as the electrode is cathodically polarized in the NO_3RR regime, which may represent a change in the local geometry coinciding with the binding of NO_3^- or NO to the Fe sites (Figure S18).

To summarize, the *in situ* XAS data suggests that the presence of Fe facilitates the electro-reduction of Mo sites in $\text{Mo}_2\text{CT}_x:\text{Fe}$ by promoting a partial defunctionalization of surface T_x groups in acidic electrolyte. In neutral media, however, Mo maintains a similar oxidation state in both $\text{Mo}_2\text{CT}_x:\text{Fe}$ and Mo_2CT_x , i.e., the surfaces of these catalysts contain a similar coverage of T_x groups. Therefore, the main difference between $\text{Mo}_2\text{CT}_x:\text{Fe}$ and Mo_2CT_x seems to lie in the fact that the presence of Fe is associated with a more disordered MXene structure that contains a higher fraction of under-coordinated Mo sites.

To gain further insights into the NO_3RR reaction mechanism on the MXene catalysts and to rationalize the promoting role of Fe in $\text{Mo}_2\text{CT}_x:\text{Fe}$, density functional theory (DFT) calculations were performed in both acidic and neutral media conditions. Our models of Mo_2CT_x and $\text{Mo}_2\text{CT}_x:\text{Fe}$ are based on XRD, elemental analysis, Fe K-edge XANES and Mo K-edge XANES and EXAFS, as well as X-ray photoelectron spectroscopy data of these materials.^[20,24,27] Considering that NH_4^+ is the major N-containing product detected here, only the reaction pathway of NO_3^- towards NH_4^+ was calculated. From Figure 3, we observe that the reaction pathways in acidic and neutral media are rather similar except in the region bound by the dashed lines. In general, the reaction proceeds via the deoxygenation of NO_3^- followed by hydrogenation in two main electrochemical processes: $^*\text{NO}_3^- \rightarrow ^*\text{NO}_2 \rightarrow ^*\text{NO} \rightarrow ^*\text{N}$ and $^*\text{NH} \rightarrow ^*\text{NH}_2 \rightarrow ^*\text{NH}_3$. Within the dashed line region, we observe that the main difference between the acidic and neutral media pathways lies in the adsorption of NO_3^- to the surface. In acidic media, NO_3^- is protonated and exists as HNO_3 , which faces a higher adsorption energy barrier on a non-substituted surface versus the Fe-substituted one. Here,

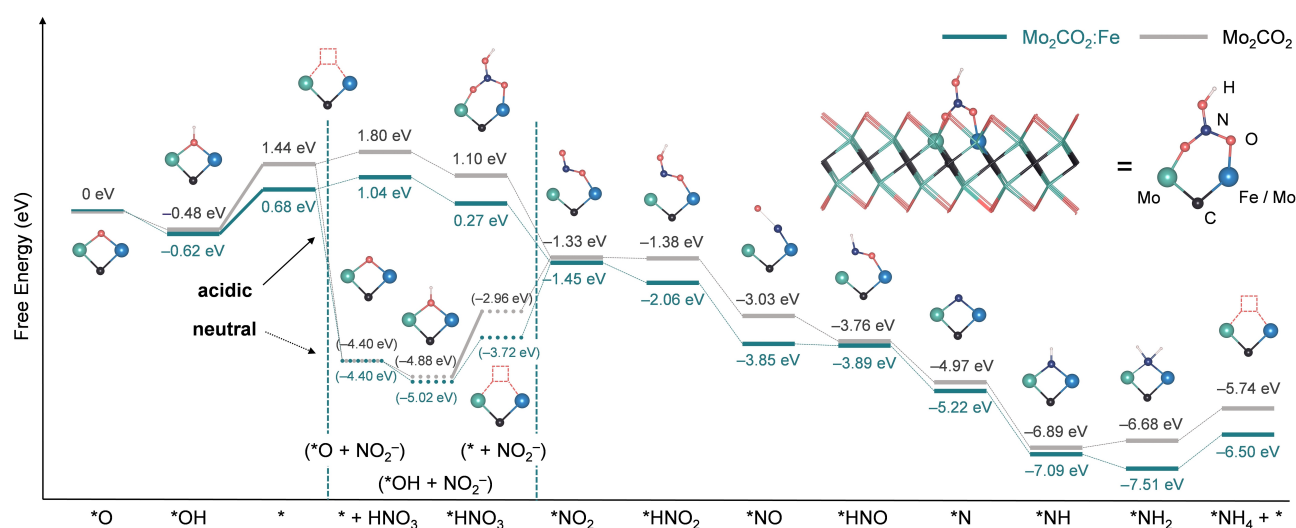


Figure 3. DFT-calculated free energy reaction pathways for the NO_3RR on Mo_2CO_2 and $\text{Mo}_2\text{CO}_2:\text{Fe}$ catalysts in acidic and neutral media.

the reaction is ultimately limited by the oxygen vacancy formation energy steps, ($\text{OH}^* \rightarrow *$, i.e. removal of T_x groups) on both surfaces. The latter step requires less energy input for the Fe-substituted material and explains its higher activity for NO_3RR . This conclusion is also consistent with the *in situ* XAS results in acidic media, which indicated that $\text{Mo}_2\text{CT}_x\text{:Fe}$ inherently features a higher fraction of T_x vacancies and a higher reducibility of Mo in the absence of a NO_3^- substrate. In contrast, in neutral media the DFT calculations suggest that NO_3^- dissociates on the MXene surface to generate NO_2^- and O^* , and this process displays similar activation energies on both Mo_2CT_x and $\text{Mo}_2\text{CT}_x\text{:Fe}$ surfaces. Nevertheless, the outcome of this dissociation step is very different on the two materials: the reaction appears limited by the oxygen vacancy formation energy step on Mo_2CT_x , (i.e. $\text{OH}^* \rightarrow *$), while on $\text{Mo}_2\text{CT}_x\text{:Fe}$ the limiting step now becomes the adsorption of NO_2^- (i.e. $\text{NO}_2^- + * \rightarrow \text{NO}_2^*$). Consequently, this observation further highlights that in both media the presence of Fe facilitates the formation of O (T_x) vacancies at the MXene surface, although via different reaction mechanisms. The appearance of these T_x vacancies is a critical step to facilitate the binding of the nitrate substrate and improving the NO_3RR performance.

Taken together, the catalytic activity data, XAS analysis, and DFT computations suggest that a key step for the NO_3RR activity of Mo-based MXene materials is the formation of O (T_x) vacancies, enabling the coordination of the substrate. This fact is in close agreement with the observations made on natural enzymatic systems, in which the protonation of the terminal Mo oxo moiety of the active site is essential to enable the binding of the substrate. The XAS and DFT studies presented herein point to the fact that the Mo centers ($\text{Mo}-\text{V}_\text{o}-\text{Mo}$) and Mo-Fe centers ($\text{Mo}-\text{V}_\text{o}-\text{Fe}$) are the sites onto which NO_3^- coordinates. In addition, both XAS and DFT highlight that in acidic media, the primary role of the Fe dopants is to facilitate the protonation of the surface oxo/hydroxo T_x sites. In that context, the Fe atoms play a similar role as the protic residues facing the Mo center in the NRase active site, further elaborating the analogy displayed in Scheme 1.

Conclusion

The electrochemical NO_3RR activities of an Fe-substituted MXene, $\text{Mo}_2\text{CT}_x\text{:Fe}$, and reference Mo_2CT_x , were evaluated in acidic and neutral media. Fe-substitution is shown to have an overall positive effect on the NO_3RR activity and the selectivity towards NH_3 production. We show that $\text{Mo}_2\text{CT}_x\text{:Fe}$ performs best in neutral media, reaching a Faradaic efficiency of up to 70 % and an NH_3 yield rate that is twice as high as that of the unsubstituted MXene. An *in situ* XAS study of the two MXene catalysts reveals that Mo sites are not reduced and remain predominantly in an oxidation state of ca. +4 under NO_3RR conditions. The *in situ* EXAFS spectra reveal that the MXene surface is partially defunctionalized and therefore contains a significant fraction of O (T_x) vacancies under NO_3RR conditions.

Ultimately, these results combined with DFT calculations show that the presence of Fe facilitates O vacancy formation, which can be correlated to the higher NO_3RR activity and NH_3 selectivity of $\text{Mo}_2\text{CT}_x\text{:Fe}$.

Acknowledgements

D.A., Y.-Z.X. and V.M. thank the European Research Council (ERC) under the European Union's Horizon 2020 research and innovation program (Grant Agreement No. 853064) for support. Dr. Agnieszka Kierzkowska (ETH Zürich) is thanked for the ICP-OES measurements. We also thank PSI for the provision of beamtime at the SuperXAS beamline (X10DA) of the Swiss Light Source (SLS).

Conflict of Interest

The authors declare no conflict of interest.

Data Availability Statement

The data that support the findings of this study are available from the corresponding author upon reasonable request.

Keywords: Ammonia · Electrocatalysis · *In Situ* X-Ray Absorption Spectroscopy · MXene · Nitrate Reduction

- [1] E. Abascal, L. Gómez-Coma, I. Ortiz, A. Ortiz, *Sci. Total Environ.* **2022**, *810*, 152233.
- [2] M. H. Ward, R. R. Jones, J. D. Brender, T. M. de Kok, P. J. Weyer, B. T. Nolan, C. M. Villanueva, S. G. van Breda, *Int. J. Environ. Res. Public Health* **2018**, *15*, 1557.
- [3] World Health Organization (WHO), *Guidelines for drinking-water quality, Vol. 1*, World Health Organization, New York, **2004**.
- [4] a) K. Parris, *Int. J. Water Resour. Dev.* **2011**, *27*, 33–52; b) S. Garcia-Segura, M. Lanzarini-Lopes, K. Hristovski, P. Westerhoff, *Appl. Catal. B* **2018**, *236*, 546–568.
- [5] M. Choudhary, M. Muduli, S. Ray, *Sustainable Water Resour. Manag.* **2022**, *8*, 113.
- [6] a) Z. Zhang, Y. Zhang, Y. Chen, *Bioresour. Technol.* **2020**, *298*, 122444; b) A. Sheik, E. Muller, P. Wilmes, *Front. Microbiol.* **2014**, *5*, 47.
- [7] P. H. van Langevelde, I. Katsounaros, M. T. M. Koper, *Joule* **2021**, *5*, 290–294.
- [8] a) X. F. Wan, W. W. Guo, X. Dong, H. H. Wu, X. F. Sun, M. G. Chu, S. T. Han, J. X. Zhai, W. Xia, S. Q. Jia, M. Y. He, B. X. Han, *Green Chem.* **2022**, *24*, 1090–1095; b) E. Murphy, Y. C. Liu, I. Matanovic, S. Y. Guo, P. Tieu, Y. Huang, A. Ly, S. Das, I. Zenyuk, X. Q. Pan, E. Spoecker, P. Atanassov, *ACS Catal.* **2022**, *12*, 6651–6662; c) Z. Y. Wu, M. Karamad, X. Yong, Q. Z. Huang, D. A. Cullen, P. Zhu, C. A. Xia, Q. F. Xiao, M. Shakouri, F. Y. Chen, J. Y. Kim, Y. Xia, K. Heck, Y. F. Hu, M. S. Wong, Q. L. Li, I. Gates, S. Siahrostami, H. T. Wang, *Nat. Commun.* **2021**, *12*, 2870; d) Y. T. Wang, C. H. Wang, M. Y. Li, Y. F. Yu, B. Zhang, *Chem. Soc. Rev.* **2021**, *50*, 6720–6733; e) J. Lim, C. Y. Liu, J. Park, Y. H. Liu, T. P. Senftle, S. W. Lee, M. C. Hatzell, *ACS Catal.* **2021**, *11*, 7568–7577;

- f) Y. T. Wang, W. Zhou, R. R. Jia, Y. F. Yu, B. Zhang, *Angew. Chem. Int. Ed.* **2020**, *59*, 5350–5354; g) Y. H. Wang, A. Xu, Z. Y. Wang, L. S. Huang, J. Li, F. W. Li, J. Wicks, M. C. Luo, D. H. Nam, C. S. Tan, Y. Ding, J. W. Wu, Y. W. Lum, C. T. Dinh, D. Sinton, G. F. Zheng, E. H. Sargent, *J. Am. Chem. Soc.* **2020**, *142*, 5702–5708; h) J. Li, G. M. Zhan, J. H. Yang, F. J. Quan, C. L. Mao, Y. Liu, B. Wang, F. C. Lei, L. J. Li, A. W. M. Chan, L. P. Xu, Y. B. Shi, Y. Du, W. C. Hao, P. K. Wong, J. F. Wang, S. X. Dou, L. Z. Zhang, J. C. Yu, *J. Am. Chem. Soc.* **2020**, *142*, 7036–7046.
- [9] T.-L. Chen, L.-H. Chen, Y. J. Lin, C.-P. Yu, H.-w. Ma, P.-C. Chiang, *J. Cleaner Prod.* **2021**, *309*, 127369.
- [10] a) D. R. MacFarlane, P. V. Cherepanov, J. Choi, B. H. R. Suryanto, R. Y. Hodgetts, J. M. Bakker, F. M. Ferrero Vallana, A. N. Simonov, *Joule* **2020**, *4*, 1186–1205; b) J. Humphreys, R. Lan, S. Tao, *Adv. Energy Sustainability Res.* **2021**, *2*, 2000043.
- [11] C. Correia, S. Besson, C. D. Brondino, P. J. González, G. Fauque, J. Lampreia, I. Moura, J. J. G. Moura, *J. Biol. Inorg. Chem.* **2008**, *13*, 1321–1333.
- [12] a) S. Al-Attar, J. Rendon, M. Sidore, J.-P. Duneau, F. Seduk, F. Biaso, S. Grimaldi, B. Guigliarelli, A. Magalon, *ACS Catal.* **2021**, *11*, 14303–14318; b) J. Rendon, F. Biaso, P. Ceccaldi, R. Toci, F. Seduk, A. Magalon, B. Guigliarelli, S. Grimaldi, *Inorg. Chem.* **2017**, *56*, 4422–4434.
- [13] M. L. Rodrigues, T. F. Oliveira, I. A. C. Pereira, M. Archer, *EMBO J.* **2006**, *25*, 5951–5960.
- [14] a) O. Einsle, A. Messerschmidt, R. Huber, P. M. H. Kroneck, F. Neese, *J. Am. Chem. Soc.* **2002**, *124*, 11737–11745; b) P. Lukat, M. Rudolf, P. Stach, A. Messerschmidt, P. M. H. Kroneck, J. Simon, O. Einsle, *Biochemistry* **2008**, *47*, 2080–2086.
- [15] Y. Li, Y. K. Go, H. Ooka, D. He, F. Jin, S. H. Kim, R. Nakamura, *Angew. Chem. Int. Ed.* **2020**, *59*, 9744–9750.
- [16] a) J. Shen, Y. Y. Birdja, M. T. M. Koper, *Langmuir* **2015**, *31*, 8495–8501; b) N. Chebotareva, T. Nyokong, *J. Appl. Electrochem.* **1997**, *27*, 975–981.
- [17] C. L. Ford, Y. J. Park, E. M. Matson, Z. Gordon, A. R. Fout, *Science* **2016**, *354*, 741–743.
- [18] a) D. H. Kim, S. Ringe, H. Kim, S. Kim, B. Kim, G. Bae, H.-S. Oh, F. Jaouen, W. Kim, H. Kim, C. H. Choi, *Nat. Commun.* **2021**, *12*, 1856; b) M. T. de Groot, M. Merckx, A. H. Wonders, M. T. M. Koper, *J. Am. Chem. Soc.* **2005**, *127*, 7579–7586.
- [19] a) Á. Morales-García, F. Calle-Vallejo, F. Illas, *ACS Catal.* **2020**, *10*, 13487–13503; b) C. Tsounis, P. V. Kumar, H. Masood, R. P. Kulkarni, G. S. Gautam, C. R. Müller, R. Amal, D. A. Kuznetsov, *Angew. Chem. Int. Ed.* **2023**, *62*, e202210828; c) B. Anasori, M. R. Lukatskaya, Y. Gogotsi, *Nat. Rev. Mater.* **2017**, *2*, 16098.
- [20] D. A. Kuznetsov, Z. Chen, P. V. Kumar, A. Tsoukalou, A. Kierzkowska, P. M. Abdala, O. V. Safonova, A. Fedorov, C. R. Müller, *J. Am. Chem. Soc.* **2019**, *141*, 17809–17816.
- [21] J. Li, C. Chen, L. Xu, Y. Zhang, W. Wei, E. Zhao, Y. Wu, C. Chen, *JACS Au* **2023**, *3*, 736–755.
- [22] a) D. Zhao, Z. Chen, W. Yang, S. Liu, X. Zhang, Y. Yu, W.-C. Cheong, L. Zheng, F. Ren, G. Ying, X. Cao, D. Wang, Q. Peng, G. Wang, C. Chen, *J. Am. Chem. Soc.* **2019**, *141*, 4086–4093; b) W. Peng, M. Luo, X. Xu, K. Jiang, M. Peng, D. Chen, T.-S. Chan, Y. Tan, *Adv. Energy Mater.* **2020**, *10*, 2001364; c) J. Zhang, Y. Zhao, X. Guo, C. Chen, C.-L. Dong, R.-S. Liu, C.-P. Han, Y. Li, Y. Gogotsi, G. Wang, *Nat. Catal.* **2018**, *1*, 985–992.
- [23] H. Zhou, Z. Chen, A. V. López, E. D. López, E. Lam, A. Tsoukalou, E. Willinger, D. A. Kuznetsov, D. Mance, A. Kierzkowska, F. Donat, P. M. Abdala, A. Comas-Vives, C. Copéret, A. Fedorov, C. R. Müller, *Nat. Catal.* **2021**, *4*, 860–871.
- [24] D. A. Kuznetsov, Z. Chen, P. M. Abdala, O. V. Safonova, A. Fedorov, C. R. Müller, *J. Am. Chem. Soc.* **2021**, *143*, 5771–5778.
- [25] Y. Li, J. Ma, T. D. Waite, M. R. Hoffmann, Z. Wang, *Environ. Sci. Technol.* **2021**, *55*, 10695–10703.
- [26] J. Yang, P. Sebastian, M. Duca, T. Hoogenboom, M. T. M. Koper, *Chem. Commun.* **2014**, *50*, 2148–2151.
- [27] a) H. Zhou, Z. Chen, E. Kountoupi, A. Tsoukalou, P. M. Abdala, P. Florian, A. Fedorov, C. R. Müller, *Nat. Commun.* **2021**, *12*, 5510; b) E. B. Deeva, A. Kurlov, P. M. Abdala, D. Lebedev, S. M. Kim, C. P. Gordon, A. Tsoukalou, A. Fedorov, C. R. Müller, *Chem. Mater.* **2019**, *31*, 4505–4513; c) J. Halim, S. Kota, M. R. Lukatskaya, M. Naguib, M.-Q. Zhao, E. J. Moon, J. Pitcock, J. Nanda, S. J. May, Y. Gogotsi, M. W. Barsoum, *Adv. Funct. Mater.* **2016**, *26*, 3118–3127.
- [28] a) Z. W. Seh, K. D. Fredrickson, B. Anasori, J. Kibsgaard, A. L. Strickler, M. R. Lukatskaya, Y. Gogotsi, T. F. Jaramillo, A. Vojvodic, *ACS Energy Lett.* **2016**, *1*, 589–594; b) S. Intikhab, V. Natu, J. Li, Y. Li, Q. Tao, J. Rosen, M. W. Barsoum, J. Snyder, *J. Catal.* **2019**, *371*, 325–332.

Manuscript received: September 14, 2023

Accepted manuscript online: October 31, 2023

Version of record online: November 15, 2023